Order-disorder effects in structure and color relation of photonic-crystal-type nanostructures in butterfly wing scales

Géza I. Márk,[1,*] Zofia Vértesy,[1] Krisztián Kertész,[1] Zsolt Bálint,[2] and László P. Biró[1]
[1]*Research Institute for Technical Physics and Materials Science, P.O. Box 49, H-1525 Budapest, Hungary*
[2]*Hungarian Natural History Museum, Baross Utca 13, H-1088 Budapest, Hungary*
(Received 4 July 2009; published 5 November 2009)

In order to study local and global order in butterfly wing scales possessing structural colors, we have developed a direct space algorithm, based on averaging the local environment of the repetitive units building up the structure. The method provides the statistical distribution of the local environments, including the histogram of the nearest-neighbor distance and the number of nearest neighbors. We have analyzed how the different kinds of randomness present in the direct space structure influence the reciprocal space structure. It was found that the Fourier method is useful in the case of a structure randomly deviating from an ordered lattice. The direct space averaging method remains applicable even for structures lacking long-range order. Based on the first Born approximation, a link is established between the reciprocal space image and the optical reflectance spectrum. Results calculated within this framework agree well with measured reflectance spectra because of the small width and moderate refractive index contrast of butterfly scales. By the analysis of the wing scales of *Cyanophrys remus* and *Albulina metallica* butterflies, we tested the methods for structures having long-range order, medium-range order, and short-range order.

DOI: 10.1103/PhysRevE.80.051903 PACS number(s): 42.66.−p, 42.70.Qs, 42.81.Qb

I. INTRODUCTION

The optical reflectance of butterfly wings often shows peculiar features, i.e., their bidirectional reflectance distribution function (BRDF) [1] is markedly different from that of simple matt "painted" surfaces, with diffuse, lambertian [2] reflectance. The most well-known optical phenomenon seen in butterfly wings is the so-called iridescence [3], when the hue of the butterfly wing changes with the angle of observation and/or illumination. Butterfly wings often have a shiny, metallic appearance, i.e., the reflectance as a function of the angle of observation has a sharp peak. Some butterflies, or beetles produce a very bright white [4,5] or very dark black [6] appearance, also the reflectance can be polarization dependent [7]. These nonlambertian BRDF functions are generally not produced by pigments, but by a microstructure or nanostructure whose optical properties change in the length scale of the wavelength of the visible (or near-UV, or near-IR) light. The specific BRDF features are produced by constructive and destructive interference of the electromagnetic waves scattered on these microstructures or nanoarchitectures. Even when the optical properties of the materials building up these nanoarchitectures do not show significant wavelength dependence in bulk form, the BRDF function of the microstructure can still show wavelength dependence. Colors produced by this mechanism are called "structural colors," or "physical colors"—in contrast to "pigmentary colors" or "chemical colors" produced by pigments. Butterfly scales are nanocomposites built of mostly two basic components (air, $n=1$ and chitin, $n=1.56$). Biological materials are always multifunctional, i.e., the butterfly wing is not only an "optical device" but has a specific aerodynamical function, and certain specialized scales are often used to distribute scents (pheromones) [8,9], and may play a role in the thermal management [10] of the animal, too. The spatial dimension of a wing scale is limited, its thickness is generally only $1-2$ μm and its lateral extension is $50-100$ μm.

Butterfly scale microstructures can be classified by a number of ways [11], a detailed classification from the point of view of biology was given by Ghiradella [12]. Very briefly, butterfly wing scales are flat sacs of dried cuticle. While the lower (closer to the wing membrane) side is generally structureless, the upper side may have a complicated structure. The most general element of this, eventually complex microarchitecture, or nanoarchitecture are regularly arranged ribs (rodlike features), running parallel with the longer axis of the scale, which may be connected by crossribs. The inside of the scale is often filled by nanostructured chitinous material, which causes [13] the structural colors. One of the simplest classification of the nanoarchitectures found in butterfly scales from a physicist's point of view is whether it has a structure in the length scale of the wavelength of visible light in one, two, or all the three dimensions (1D, 2D, and 3D structures). If this spatial variation is periodic (or quasiperiodic), the structure may be called a photonic crystal as introduced by Yablonovitch [14]. 3D photonic crystals are found in the scales of many butterflies [15–19]. In a very suggestive way, entomologists called the scanning electron microscopy (SEM) images of certain kind of 3D nanostructures "pepper-pot" structure [20] to designate a structure resembling that of inverted opal.

Direct access to the 3D microstructure is possible by electron tomography [21,22] and even by x-ray tomography [23] but the practical and widespread application of these methods would require a significant improvement in technology. Most important tools to analyze the microstructure of butterfly wing scales are SEM and transmission electron microscopy (TEM). Top-view SEM images provide information, however, about the topmost layer only and the sample prepa-

*mark@sunserv.kfki.hu; http://www.nanotechnology.hu

ration (deposition of sputtered gold) may distort the appearance of the nanostructures on the images. Cross-sectional TEM images do give access to the in-depth structure of the scales, but the precise direction of the cut is generally not known—an uncertainty of 5–10° is common— and the samples are sometimes distorted during the preparation process. Both methods give basically 2D information and it is a non trivial task to determine the real 3D structure of the scale based on SEM and TEM images.

A careful correlated examination of the SEM and TEM images [18] has to be carried out in order to obtain the full 3D structure. Recently Stavenga *et al.* [24] showed, by an analysis of formerly published SEM and TEM images that several of the 3D cuticular structures in the lycaenid and papilionid species can be modeled by a so called gyroid structure, a bicontinuous triply periodic structure with a body-centered cubic (BCC) Bravais lattice symmetry.

As shown in the theory of photonic crystals [25], only 3D photonic crystals can have a complete photonic band gap (PBG), but because of the moderate refractive index contrast and also of the small thickness in butterfly wings the PBG is generally not "perfect," i.e., the reflectance in the PBG wavelength range is no 100%. Crystalline order, however, is not a necessary condition of the existence of PBG, amorphous materials can also have a PBG [26] independent of incident direction, if a short-range order is present.

It is remarkable, however, that not only nonlambertian BRDF functions, but also lambertian ones (i.e., those having an appearance of a normal matt surface) can be produced by scale microstructures [18]. Metallic-like reflectance, i.e., emergence angle selection is related to the photon momentum conservation, which follows from total or partial translational invariance in the diffusing surface structure. Hence the metallic-like reflectance is associated with highly correlated structures [3,17]. Lambertian scattering, by contrast, seems to always involve some form of long-range disorder. As we have shown recently [18], the very same butterfly can show both phenomena—shiny and matt reflectance—both as a result of microstructure. Indeed, the dorsal scales of the butterfly *Cyanophrys remus* are photonic single crystals of dimension 50×120 μm^2—this is responsible for the metallic blue appearance of the dorsal wing—while the color generating scales on the ventral wing surface are photonic polycrystals, i.e., an assembly of photonic crystallites of micron size, with a random long-range distribution in the orientation of the grains, this is responsible for the matt green color of the ventral wing. Both the shiny reflectance and the diffuse reflectance have specific biological function for the individual. Shiny dorsal reflectance is used for signaling, which is crucial for sexual communication, therefore the color is under sexual selection. The ventral matt color has a cryptic function serving as a generalized camouflage function, thus affected by natural selection [27].

To be able to get deeper insight in the intricate ways, in which natural evolution structured the photonic crystal type nanoarchitectures even when these nanoarchitectures do not exhibit a long range order, we developed an analytical method. This method will be presented in the paper by applying it to two butterfly species we investigated earlier, both of them exhibiting blue and green colors originating from photonic nanoarchitectures: *Cyanophrys remus* [18] (dorsal: shiny metallic blue, ventral: matt green) and *Albulina metallica* [19,28] (dorsal: blue, ventral: silvery green).

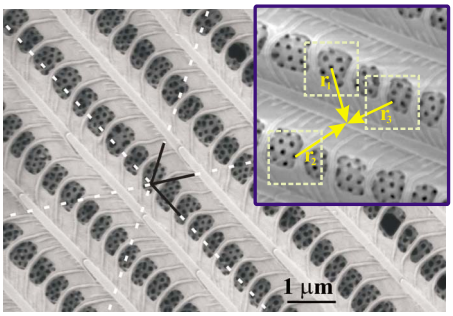

FIG. 1. (Color online) Scanning electron microscopy image of a dorsal wing scale of *Cyanophrys remus*, from Ref. [18]. The white and black lines at 60° rotations were inserted to help the eye to recognize the long-range order. The inset illustrates the real space averaging algorithm (see text for details).

The organization of the paper is as follows. In Sec. II, the real space averaging method is introduced. In Sec. III, we apply the method to three characteristic examples, one possessing long range periodicity (*Cyanophrys remus* dorsal wing surface), another with medium range order (*Cyanophrys remus* ventral wing surface), and one with short-range order (*Albulina metallica*). It will be discussed in detail in this section, how the randomness, which is inherently present in the nanoarchitectures of biological origin, influences the light scattering process. In Sec. IV, we turn to the investigation of TEM sections and their Fourier images. By systematic analysis of different distortions of a perfect lattice we identify the signatures of disorder in the Fourier power spectrum. This Section contains a modified version of the method of Prum [29] to predict the spectrum from the Fourier image. Section V is devoted to the discussion of the results.

II. DIRECT SPACE AVERAGING METHOD

Because of their very biological origin, butterfly wing structures are not as regular, as crystals in solid state physics. In order to determine the characteristic symmetries and dimensions of these structures with good statistics, it is necessary to perform tedious measurements on the SEM and TEM images. Fourier transform, as a mathematical tool is widely used to reveal the periodicities in a structure. This is very useful, when the long-range order is disturbed by a short-range disorder or there are several periodicities present in the structure. Both of these factors are in fact present on the SEM images of the dorsal scales of *Cyanophrys remus*, as shown on Fig. 1. It is not an easy task to recognize the long range periodicity of the pepper-pot structure on this image by mere visual observation. Fourier analysis, however, clearly shows (see Fig. 6 of [18]) that the reciprocal space image is a convolution of a smaller scale triangular structure (corresponding to the small holes) and a larger scale rectangular structure (corresponding to the windows).

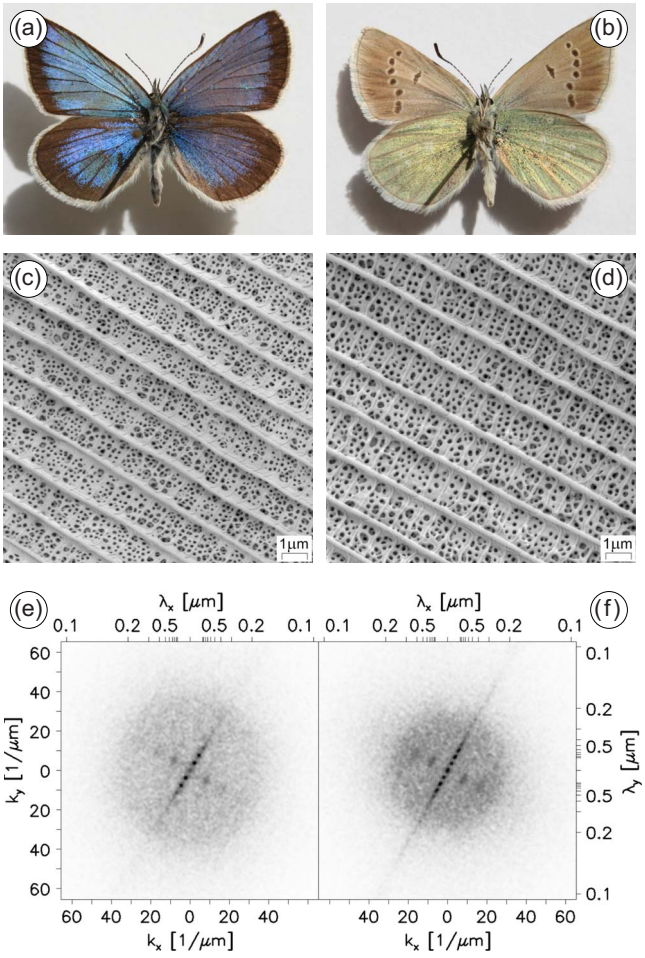

FIG. 2. (Color online) Comparison of the dorsal and ventral wing surface of the *Albulina metallica* butterfly. (a) and (b) Optical images. (c) and (d) Scanning electron microscopy images. (e) and (f) Two-dimensional Fourier power spectrum of the SEM images shown on (c) and (d). White corresponds to zero intensity and black to maximum intensity. Wave number (wavelength) scale is shown on the lower and left (upper and right) axis, respectively.

Reciprocal space methods give information about the periodic structures building a photonic crystal and also provide a quantitative measure of the irregularity of the structure. The Fourier method, however, is effective only if the image does have a long range order. Moreover the Fourier technique requires a SEM image containing a fairly large number of spatial periods, which is often not available on micrographs of butterfly scales.

Figures 2(a) and 2(b) shows photos of the dorsal and ventral wing surfaces of the butterfly *Albulina metallica*. The dorsal surface has a blue coloration, while the ventral side is silvery green. Despite this difference of the visual appearance of the two wing sides, at the first glance no characteristic difference is seen between the SEM images of the dorsal (ventral) sides, cf. Fig. 2(c) and 2(d). Neither the Fourier transform of these SEM images, Figs. 2(e) and 2(f), shows a marked difference, though we recorded special, large size (12×12 μm^2), and high-resolution (2048×2048 pixel) SEM images in order to provide good accuracy of numerical Fourier transformation. The reciprocal space images (Figs. 2(e) and 2(f)) have a similar structure. The series of strong black dots arranged in a line, with direction perpendicular to the direction of ridge lines seen in Figs. 2(c) and 2(d) correspond to the regular series of ridges. Apart from the first order peaks the 2nd and 3rd order peaks have a large amplitude because of the anharmonicity of the ridge structure. The series of gray dots arranged in a line perpendicular to the line of the strong black dots correspond to the crossribs. These dots have a smaller amplitude and larger spread because the arrangement of the crossribs is not as regular as that of the ridges. Both Fourier images show a diffuse gray disk centered at the origin. These disks correspond to the array of the small holes (i.e., to the pepper-pot structure). No inhomogeneities can be seen in the disks, apart from the random fluctuation, which shows that there is no long-range order in the pepper-pot structure. The fact that the diameter of the disks is finite indicate, however, the presence of a length scale in the pepper-pot structure, i.e., the presence of a lower limit for the distance of the small holes. The diameter of the gray disk on Fig. 2(e) [dorsal fast Fourier transform (FFT) image] is larger than that on 2(f) (ventral FFT image), which shows that the lower limit for the hole distance is smaller on the dorsal wing surface SEM image than on the ventral wing surface SEM image. This is in accordance with the visual appearance of the two wing sides: the dorsal side (with smaller average hole distance) is blue, while the ventral side (with larger average hole distance) is green. (As it is shown in Sec. V, the average refractive index is nearly the same for the two sides.)

In order to study the local order in TEM and SEM images of butterfly scales, we have developed a simple direct space algorithm, based on averaging the local environments of the scattering sites. The method provides the statistical distribution of the local environments, including the histogram of the nearest-neighbor distance and the number of nearest neighbors.

The direct space averaging method assumes that the SEM image of the 3D microstructure contains repetitive units. In the case of pepper-pot structures the repetitive units are the small, dark holes seen on the SEM images This generally applies to the SEM images of butterfly scales containing pepper-pot nanostructures, see Fig. 1 for a characteristic example.

The algorithm of the direct space averaging method is as follows:

(i) FOR each hole
  (a) FIND center of the hole: $\vec{r}_{hole}$
  (b) SHIFT the image with $\vec{r}_{shift}=-\vec{r}_{hole}$
(ii) AVERAGE gray values of all shifted images

The algorithm is illustrated on the inset of Fig. 1. It shows a detail of the SEM image of Fig. 1. The arrows pointing from three, arbitrarily selected holes to the origin show the $\vec{r}_{shift}=-\vec{r}_{hole}$ vectors, along which the image is shifted such that the center of the corresponding hole is translated into the origin. In the real algorithm this hole selection and image shift operation is repeated for all the holes found on the image. The first step, the finding of the center of each holes is performed by first binarizing the image (after an application of a moderate amount of median and smoothing filtering) then by determining the center of gravity of the holes.

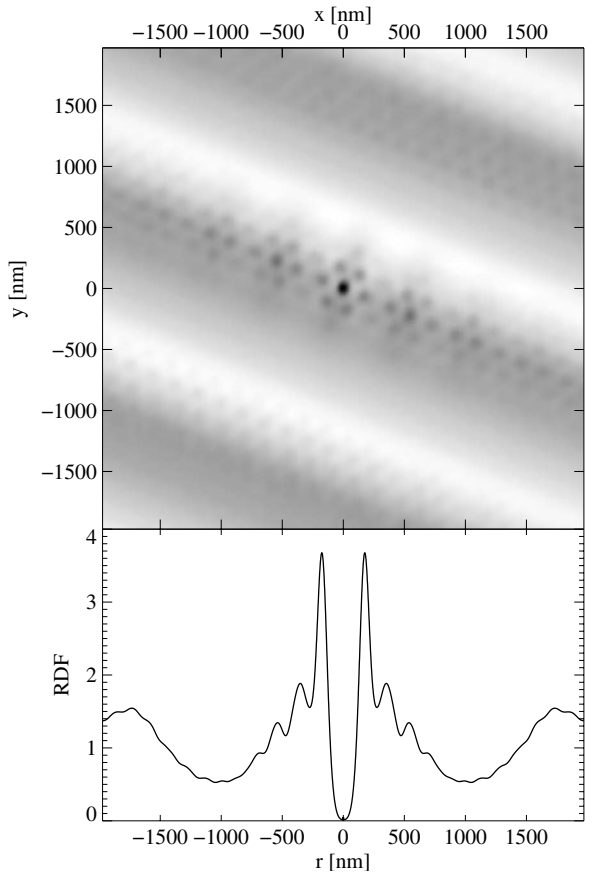

FIG. 3. (a) Result of the real space averaging algorithm for the SEM image of a dorsal wing scale of *Cyanophrys remus*. Note the hexagonal arrangement of the nearest neighbors and the long-range correlation between the different windows and between the neighboring window rows. (b) Radial distribution function of the center points of the holes seen on the SEM image of the dorsal wing scale of *Cyanophrys remus*.

SEM images are finite rectangular arrays of pixels and we have to decide how to handle the effect of the edges of the images during the shift operation. A suitable solution is not to shift the whole image, just only a subimage centered on the hole under processing. After determining the $\vec{r}_{hole}$ position of a given hole, we cut a small square window centered on the hole out of the SEM image. The size of this window has to be about $10a$ for pepper-pot structures possessing long-range order (e.g., *Cyanophrys remus*, cf. Fig. 3) and about $4a$ for those of short range order (e.g., *Albulina metallica*, cf. Fig. 5), where a is the average distance of the holes, its typical value is 200 nm. Those holes closer the edge of the image than the half of the small window size are left out of the averaging. For real SEM images of butterfly scales this solution is perfectly suitable, because the SEM images are much larger, than the size of the small window, hence, only a thin border region is left out of the averaging.

III. APPLICATION OF DIRECT SPACE AVERAGING

A. Long-range order

Figure 3 shows the result of the above described real space averaging method for the dorsal wing surface SEM image of the butterfly *Cyanophrys remus*, together with the radial distribution function (RDF) of the center of the small holes. Although the long-range order of the small holes is only visible by a careful observation on the SEM image itself, cf. Fig. 1 the presence of the long-range order becomes obvious on the real space averaged image. Indeed, the correlation is present for more than 10 neighbors and it is even seen between windows separated by the ridges. The small holes clearly form a triangular lattice, i.e., each hole has six nearest neighbors placed on the vortices of a regular hexagon. The RDF function is zero for small distances, which shows that the holes "does not like" to come close to each other. There is a sharp and high nearest-neighbor peak, the second and third neighbor peaks are also pronounced. The higher order peaks, which are very well seen on Fig. 3(a) are suppressed on the RDF function by the azimuthal averaging. The wide peak seen at 1700 nm corresponds to the correlation of the windows between neighboring window rows (separated by a ridge). One can see small peaks on the top of the wide peak, this shows the presence of the correlation between the small holes seen in the neighboring ridge rows, as it is also very well seen on Fig. 3(a). No random noise is visible on the RDF function, this is because of the good long range correlation and the large integrating area.

B. Medium range order–granular structure

The wing scales on the ventral side of the *Cyanophrys remus* butterfly have a granular structure, as it was analyzed in detail in [18]. As we have shown in [18] the ventral scales are "photonic polycrystals" composed of crystallites with 3–5 μm typical lateral diameter. TEM images (cf. Fig. 7 of [18]) clearly show a crystalline order within each grain. On the SEM image, Fig. 4(a), however, it is not so obvious to note the ordered structure, because of the ridges and cross-ribs and also of the random disorder. Direct space averaging "transforms out" these two factors, hence the crystalline order becomes obvious on the direct space averaged images, Fig. 4(b). The different subimages show different symmetries and orientations, which correspond to different lattice planes of a 3D crystalline lattice. The reflected colors computed for these lattice planes were identified experimentally by optical microscopic investigation of the scales [18]. Combined effect of different colors gives the matt appearance.

C. Short-range order

Figure 5 shows the result of the real space averaging method for the dorsal and ventral side SEM images of the *Albulina metallica* butterfly, together with the RDF of the small holes. We can see that, contrary to the case of Secs. III A and III B only the first neighbor shell shows a good radial correlation, though the second and third neighbor peaks are also visible on the RDF function. Random noise on these images is more pronounced than on Fig. 3 because of the lack of long range order.

When comparing the dorsal and ventral wing surfaces, the position of the first neighbor peak is at 209 nm for the dorsal, and at 261 nm for the ventral case (see Table I for details).

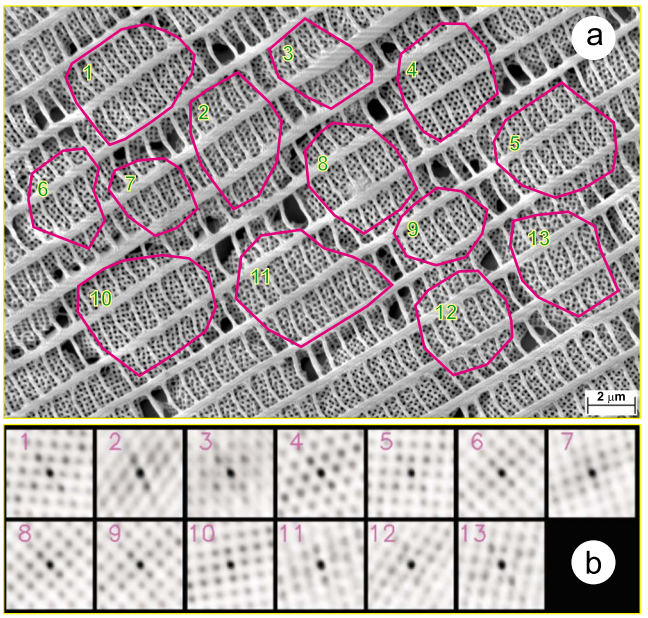

FIG. 4. (Color online) (a) Scanning electron microscope image of the grain structure seen on a ventral scale of the *Cyanophrys remus*. The numbered contours show the regions selected for direct space averaging. (b) Results of direct space averaging for the numbered regions from (a). Note the different ordered structures.

The first neighbor peak is more pronounced at the dorsal side. The angular correlation is also much weaker in the case of *Albulina metallica* than for the *Cyanophrys remus* but we can see slightly larger angular correlation of the first neighbors on the ventral side than for the dorsal. The peak at 700 nm on the ventral RDF function corresponds to the correlation of the windows separated by crossribs, this is not so pronounced on the dorsal side.

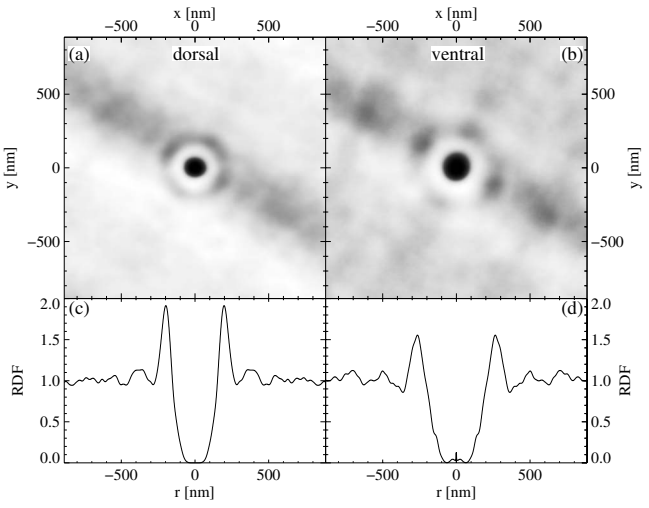

FIG. 5. (a) and (b) Result of the real space averaging algorithm for the SEM image of a dorsal (ventral) wing scale of *Albulina metallica*. Note the presence of short range order and the lack of long range order. (c) and (d) Radial distribution function of the center points of the holes seen on the SEM image of the dorsal (ventral) wing scale of *Albulina metallica*.

IV. ESTIMATION OF THE REFLECTANCE SPECTRUM

A. Analysis of the TEM images

In order to reveal the in-depth structure of the scales, TEM investigations were taken, Fig. 6 shows the TEM results for the dorsal and ventral scales. In the interpretation of the TEM images one has to have in mind a number of particularities of TEM sample preparation, discussed to great detail in [18]. Briefly:

(i) The object of study has to be produced as a section of around 100 nm thickness (70 nm in our work) to make it transparent for the electrons.

(ii) This is achieved by incorporating the object in a special resin followed by ultramicrotoming with a diamond knife (both faces of the slice are produced by cutting), the shear to which the thin slice is subjected during this process is rather high, it often causes the exfoliation of the resin from the object.

(iii) Due to the slice thickness, to the high shear and due to the fact that the dimensions of the walls separating the holes are in the range of 80–90 nm, a cutting plane even marginally misplaced from the line rigorously joining the centers of the adjacent holes can result in several solid regions separating adjacent holes being missing.

(iv) Even when the little "column" joining two adjacent filled layers in the TEM image is missing its "footprint" can be identified as undulations of the upper/lower layers.

On Figs. 6(c) and 6(e) the cutting was done perpendicular to the ridges, indeed, the dorsal and ventral ridge distances measured on these TEM images match that resulting from the SEM images (cf. Table I). The circular holes indicate the presence of some hollow spatial structure, whose cross section is circular. On Figs. 6(d) and 6(f), however, the apparent ridge distances are about 1.7 times larger, but the layer distances are still comparable with that measured on Figs. 6(c) and 6(e). Note that the ridges on Figs. 6(d) and 6(f) are not only farther away, but also have an elongated shape, as compared with that on Figs. 6(c) and 6(e). These findings can be understood if we suppose that the sections imaged on d and f were cut not perpendicular to the ridges but under a certain angle, see Figs. 6(a) and 6(b) for illustration. Note, however, that the small holes on Figs. 6(d) and 6(f) are not elongated along the lateral direction, as they should appear, if, for example the hollow spaces were cylindrical. Moreover, the average lateral hole distances on Figs. 6(c) and 6(e) match those measured on Figs. 6(d) and 6(f), respectively. The fact, that the holes are circles among the Figs. 6(c), 6(e), 6(d), and 6(f) images can be explained if we suppose that the hollow spaces are spherical air holes, or bubbles inside the chitin matrix. The size of the holes, however, is varying on the TEM images. This is caused by the random arrangement of the air spheres, the cutting plane intersects the spheres at different positions. The apparent density (gray level) of the wall between the spheres is also varying in the lateral direction, from the black through gray to completely white. This is caused by the finite thickness of the cut slice. The interlayer boundaries are nevertheless always completely dense (black) on the TEM images, this shows that the transversal order is larger than the lateral order, i.e., the spheres are

TABLE I. Results of distance measurements performed on the micrographs of the wing scales of *Albulina metallica*. "Ridge:" distance of the ridges, "hole RDF:" distance of the holes calculated from the RDF function, "layer;" layer distance, "lateral upper:" distance of the holes in the upper layer.

Method	Quantity	Dorsal average	Dorsal stdev	Ventral average	Ventral stdev
SEM	Ridge	1430	123	1685	169
SEM	Hole RDF	209	49	261	64
TEM	Ridge	1252	92	1580	80
TEM	Layer	203	38	257	29
TEM	Lateral upper	200	29	272	62

arranged into layers but they are randomly distributed inside the layers.

As we can see in Table I, the average lateral interhole distances measured on the dorsal and ventral TEM images match the first neighbor positions of the dorsal and ventral SEM. RDF functions, see Fig. 5. These numbers in turn match the interlayer distances measured on the TEM images, see Table I.

B. Ewald sphere approximation

Prum *et al.* [29] proposed a simple and universal procedure of estimating the reflectance spectrum from the TEM images. They first calculate the two-dimensional Fourier power spectrum (2D FFT) of the binarized TEM image then they estimate the reflectance spectrum by angular averaging of the power spectrum for the whole $[0,2\pi)$ range or for $\pi/6$ wide sections. This heuristic approach is based on basic scattering theory [30]. The scattering intensity is given by

$$I(\vec{k};\vec{k}_0) = \int \rho(\vec{r})\exp\left(i\frac{\vec{q}}{n_{eff}}\vec{r}\right)d^D\vec{r}, \qquad (1)$$

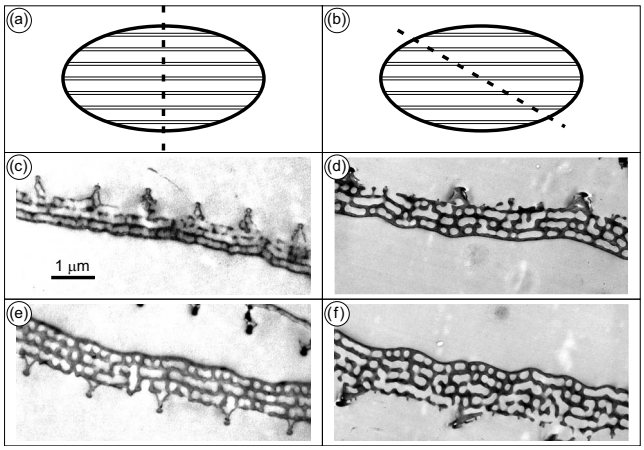

FIG. 6. Cross-sectional transmission electron microscopy images through the wing scales of *Albulina metallica*. TEM images in the left column were made on a section perpendicular to the ridges and to the scale surface, as illustrated in (a), TEM images in the right column were made on a section at an oblique angle to the ridges but perpendicular to the scale surface, as illustrated in (b). (c) and (d) Dorsal scales. (e) and (f) Ventral scales. For results of distance measurements performed on these images, see Table I.

where $\rho(\vec{r})$ is the density of scattering centers, $\vec{k}_0$ is the wave vector of the incoming light, $\vec{k}$ is the wave vector of the outgoing (reflected or transmitted) light ($|\vec{k}_0|=|\vec{k}|=2\pi/\lambda$ in case of elastic scattering), $\vec{q}=\vec{k}-\vec{k}_0$ is the scattering vector, and n_{eff} is the effective refractive index of the medium. The integral is a D dimensional integral, $D=3$ in 3D calculations, but $D=2$ if the scattering is considered only in a plane, as was done in [29]. This equation can be graphically demonstrated by the so called Ewald construction, see Fig. 7, which is widely used in the theory of X-ray scattering. See Sec. V for a detailed analysis of the approach used in [29].

C. Signatures of disorder in the Fourier power spectrum of TEM images of butterfly scales

If a structure has a perfect long range order, its Fourier transform is composed of distinct peaks. This situation, illustrated in Fig. 8(b) is seen in x-ray scattering images in solid state physics, because atomic or molecular crystals have very regular structures. If the real space structure is not as regular as crystals in solid state physics, as is the case in biological systems, the Fourier transform is not any more composed of Dirac delta like peaks, but it has a complicated, continuous distribution in reciprocal space. The denomination "randomness," however, is not well defined, there can be several kinds of "randomnesses" present in the image, hence a care-

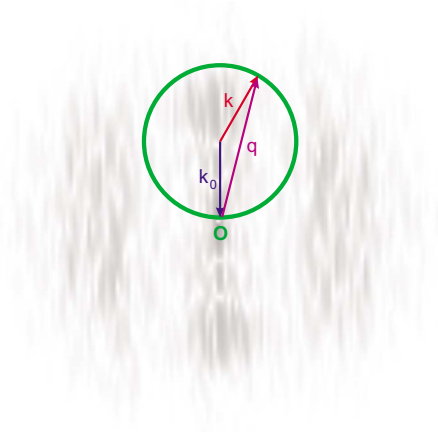

FIG. 7. (Color online) Ewald sphere construction illustrated for the case of a two-dimensional Fourier power spectrum of a TEM image. A case of perpendicular light incidence ($\vec{k}_0$) and oblique observation ($\vec{k}$) is shown. See the text for details.

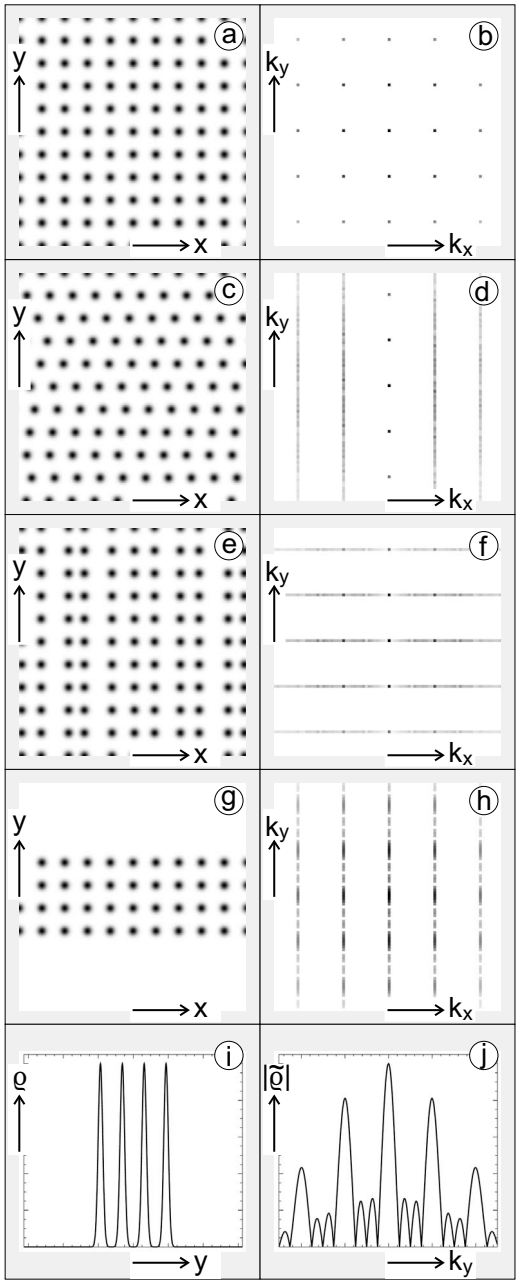

FIG. 8. Effect of randomness and of the finite number of layers on the Fourier power spectrum. (left) Real space images. (right) Reciprocal space images. (a) and (b) Perfect rectangular lattice. (c) and (d) Random horizontal displacement of the layers. The lattice is perfect inside each layer. (e) and (f) Random horizontal displacement of the lattice sites inside the layers. The layers are identical. (g) and (h) Four layers, perfect rectangular lattice. (i) and (j) The vertical density distribution (ρ) and Fourier power density distribution ($|\tilde{\rho}|$) in the central column ($x=0, k_x=0$) of (g) and (h). Dimensionless units are used in all subimages. See the text for details.

ful analysis is necessary to separate the different effects. Figure 8 demonstrates the effect of some characteristic randomnesses on the Fourier image. Real butterfly scales are 3D structures, but we used 2D lattices to demonstrate the different "randomnesses" in this Subsection, because it is easier to demonstrate the phenomena in 2D and these same phenomena are present in 3D.

Figure 8(a) shows a rectangular section of a perfectly regular and infinite 2D square lattice. Its Fourier power spectrum, shown on Fig. 8(b), is a square lattice of distinct peaks. The intensity of the peaks is decreasing with the distance from the origin, this decrease is faster if the objects placed on the lattice points of the real space lattice are larger. As we know from the theory of x-ray scattering, if N objects of density $\varrho(\vec{r})$ are placed in the points of the direct space lattice $\{\vec{r}_i\}_{i=1}^N$, the total scattering of the system is given as the product of the lattice factor (Fourier transform of the lattice) and the so called atomic form factor (Fourier transform of $\varrho(\vec{r})$). The Fourier image is composed of distinct peaks in the horizontal (vertical) x (y) direction if the lattice has a long range order in the x (y) direction.

Figure 8(c) shows the same lattice, but each lattice layer is randomly displaced horizontally. We can see in Fig. 8(d) that the Fourier image is composed of vertical lines. This is because the random displacement of the layers destroys the perfect translational symmetry in y. The image is still composed of discrete lines, because the layers still have a perfect translational order in the x direction.

Figures 8(e) and 8(f) shows the effect of the disorder present in the layers themselves. This time a random horizontal displacement (with a Gaussian distribution) was applied to the points of one layer and this layer was repeated infinitely in the y direction, the layers have the same structure. The Fourier image shows distinct horizontal lines. Indeed, each reciprocal lattice point is broadened in the x direction because of the random x displacement of the points, but the translational order is present in the y direction because the layers have an identical structure.

It was assumed so far, that the direct space lattice is infinite. Figure 8(g) shows the effect of the spatial confinement of the system, it is composed only of four layers, but the layers are assumed to be infinite in the x direction. As seen on Fig. 8(h), the Fourier peaks are broadened in the y direction and satellite peaks appear between the original peaks. This is caused by the vertical confinement of the system. Indeed, a finite lattice of n_l layers in the vertical direction can be described as

$$\rho(y) = p(y)\Theta(y;n_l), \tag{2}$$

where $p(y)$ is a periodic function with period a and $\Theta(y;n_l)$ is a square window function of n_l periods width, defined as

$$\Theta(y;n_l) = \begin{cases} 1, & \text{if } |y| < an_l/2; \\ 0, & \text{otherwise} \end{cases}. \tag{3}$$

Utilizing the convolution theorem we receive the Fourier transform of $\rho(y)$ as follows

$$\tilde{\rho}(k) = \sqrt{\frac{2}{\pi}}\frac{1}{\omega}\sum_{j=-\infty}^{\infty} c_{n_l j}\frac{\sin\pi\left(\frac{k}{\omega}-n_l j\right)}{\frac{k}{\omega}-n_l j}, \tag{4}$$

where $\omega=2\pi/a$ and the c_i are the quotients of the Fourier series of the periodic function $p(y)$. Taking into account that the $\sin\pi(k/\omega)/(k/\omega)$ kernel has zero nodes at $\pm\omega, \pm 2\omega, \ldots$ there are n_l-1 zero nodes and n_l-2 extrema between $n_l j$ and

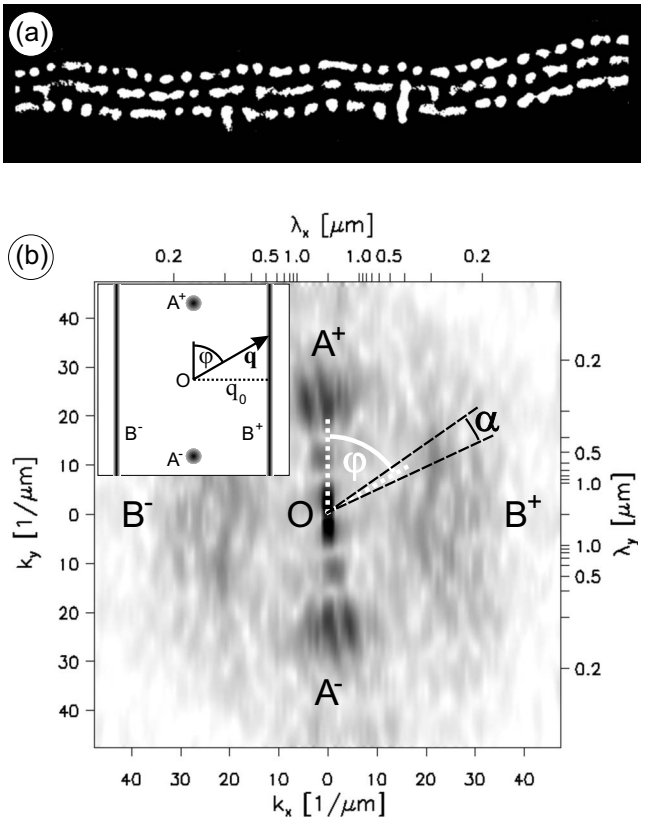

FIG. 9. (a) Processed cross-sectional transmission electron microscopy image through a ventral scale of *Albulina metallica*. A background correction and a binarizing filter was applied to the image on Fig. 6(e) (see the text for details). (b) Fourier power spectrum of the processed TEM image shown in (a). White corresponds to zero intensity and black to maximum intensity. Wave number (wavelength) scale is shown on the lower and left (upper and right) axis, respectively. The lines illustrate the procedure of the calculation of the backscattered spectrum from the Fourier image. The inset shows the Fourier image and the procedure of the spectrum calculation for a model image, Fig. 8(c).

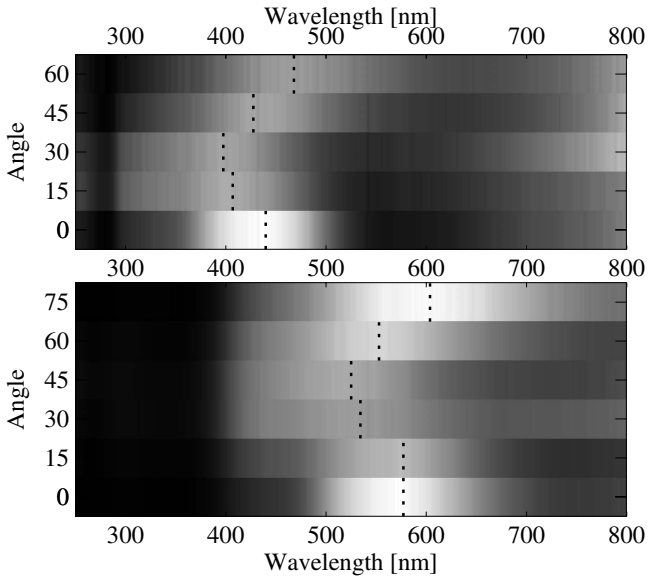

FIG. 10. Reflectance spectra of the *Albulina metallica* wings recorded at backscattering arrangement at several angles. All spectra were measured relative to a diffuse white standard. Black corresponds to zero intensity and white to maximum intensity. A nonlinear gray scale is used to facilitate presentation. Black dotted lines show the wavelengths with maximum intensity for each angle. (Upper) dorsal wing surface and (lower) ventral wing surface.

$n_l(j+1)$. This is illustrated in Figs. 8(i) and 8(j), Fig. 8(i) shows a function constructed as a sum of four Gaussians placed on an equidistant grid and Fig. 8(j) shows its Fourier power spectrum. We can see three zero nodes and two maxima—exactly as in Fig. 8(h).

This all said we are in the position to understand the Fourier image of a real sample. As it was explained earlier (see Sec. IV A), the apparent density of the walls between the holes is varying because of the TEM sectioning process. In order to compensate this artifact we processed the TEM image of the ventral scale (Fig. 6(e)) by a background correction and a binarizing filter. The resulting black and white image is shown in Fig. 9(a). Figure 9(b), is the Fourier power spectrum of the so constructed direct space image. The vertical structure A^-–O–A^+ corresponds to the layer structure, cf. Figs. 8(i) and 8(j). Note that there are two minima and one maximum between each pair of main peaks, which corresponds to the presence of three layers. The peaks at A^-,A^+ are broadened horizontally because the layers are not perfectly flat but wavy. The vertical bars at B^-,B^+ correspond to the lateral order of the holes, cf. Figure 8(b). These Fourier peaks have a finite thickness in both the horizontal and vertical direction because the holes are randomly arranged in the layers [cf. Figure 8(e)] and the layers have different microstructure [cf. Figure 8(c)].

D. The reflectance spectrum

Figure 10 shows the $I(\lambda,\varphi)$ reflectance spectrum of the dorsal and ventral hindwing of the *Albulina metallica* butterfly (cf. Figure 2) measured in a backscattered configuration for the $(0°-60°)$ angle range for the dorsal wing and for the $(0°-75°)$ angle range for the ventral wing. Reflection peaks measured on butterfly scales are always broadened, because, on one hand, the structure has a randomness in the lattice (cf. Table I), and because, the scales are not flat, on the other hand. This latter factor is very well seen on the large scale TEM image shown on Fig. 11. The $\lambda_{max}(\varphi)$ wavelength values belonging to the maximum intensity are given in Table II and are shown by dotted lines in Fig. 10. Both the dorsal and ventral $\lambda_{max}(\varphi)$ functions have a similar structure: $\lambda_{max}(\varphi)$ is first decreasing with increasing φ, then it is again increasing.

V. DISCUSSION

The simple theory of reflectance spectrum calculation based on Eq. (1) is valid with the assumptions that (i) the incoming light is directly scattered on each inhomogeneity of the $n(\vec{r})$ complex optical index function; (ii) each scattered wave is directly going into the detector; and (iii) no intensity loss of the incoming and scattered waves occur. These assumptions, generally called first Born approximation, are

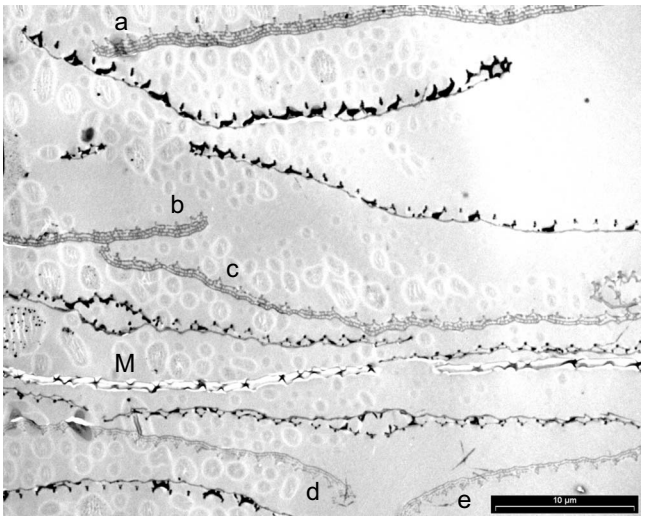

FIG. 11. Large scale cross-sectional transmission electron microscopy image through the wing scales of *Albulina metallica*. The thick surface, denoted by letter "M" crossing horizontally through the image is the wing membrane. Both the dorsal and ventral side of the wing is seen, there are three dorsal scales (a, b, and c) and two ventral scales (d and e) with photonic nanostructure on this large scale image. Note that the scales are curved.

valid if the thickness of the system is small and the optical index contrast is small. These assumptions are fulfilled in the case of butterfly scales, with an optical index contrast of $n_{chitin}/n_{air}=1.56/1$ and a thickness of $1-2$ μm. Multiple scattering is negligible in such systems in general, as validated by transfer matrix theory [13,18] and finite difference time domain (FDTD) calculations. The scales of many Lepidoptera and the elytra of quite a number of Coleoptera possess specialized micro and nanostructures that produce polarization effects [7]. In most insects, the structure is locally symmetric; hence, no macroscopic effects can be seen. In certain species, this symmetry is partly broken, and a polarization-dependent reflection can be observed [31]. No such symmetry breaking is present in *Albulina metallica*, hence, and unpolarized calculation based on Eq. (1) describes the reflection sufficiently.

According to Eq. (1), if an incoming plane wave of $\vec{k}_0$ wave vector is scattered into the plane wave of $\vec{k}$ wave vector, then the scattered intensity $I(\vec{k}_0;\vec{k})$ is simply proportional with the value of the 3D Fourier power spectrum at the point $\vec{q}/n_{eff}$, where $\vec{q}=\vec{k}-\vec{k}_0$, as is graphically illustrated in Fig. 7. The situation is especially simple in case of a backscattering geometry, when $\vec{k}=-\vec{k}_0=\vec{n}2\pi/\lambda$, where $\vec{n}$ is the direction of the scattering, because the scattering vector is $\vec{q}=2\vec{n}2\pi/\lambda$.

For the case of normal backscattering from the ventral wing surface of *Albulina metallica* we have to simply take into account the intensity distribution ("line cut") of the 3D Fourier power spectrum (cf. Figure 9) along a vertical line crossing the origin. The most pronounced peak is at $A^{\pm}$, which is corresponding to the layer distance d_{layer}, i.e., $OA^{\pm}=2\pi/d_{layer}$. Hence, the peak position in $I(\lambda)$ is at $\lambda_{layers}=2n_{eff}d_{layer}$. This is the familiar formula for 1D photonic crystals (multilayers). Assuming a 2D close packed arrangement of spheres inside layers and a simple stacking of the layers in z direction the filling ratio of the spheres is $V_{sphere}/V=\pi/(3\sqrt{3})$, and

$$n_{eff}=n_{air}V_{sphere}/V+n_{chitin}(1-V_{sphere}/V)\cong 1.22.$$

Replacing layer distances from Table I we receive

$$\lambda_{dorsal}^{normal}=2\times 1.22\times 203=495 \text{ nm} \quad (5)$$

$$\lambda_{ventral}^{normal}=2\times 1.22\times 257=657 \text{ nm}.$$

These numbers overestimate those measured at normal direction backscattering (cf. Figure 10 and Table II) by 15% which is due to the fact that, as seen on SEM images (cf. Figure 2), the chitin membrane between the layers of spheres is a not continuous, holey structure. Inserting $n_{eff}^{dorsal}=1.08$ and $n_{eff}^{ventral}=1.12$ gives the measured wavelengths.

Next we turn to the study of the goniometric backscattered spectra shown on Fig. 10. Only the analysis of the ventral results is given here, the trend of $\lambda_{max}(\varphi)$ is similar on the dorsal and ventral side, only the wavelength values are smaller (cf. Table II). Prum *et al.* assumed that the density of light scattering centers (the quantity, that has to be inserted into Eq. (1)) is identical with the binarized gray value seen in TEM images,

$$\rho^{ligh\ \ scattering\ \ centers}=\text{bin}(\rho^{TEM}). \quad (6)$$

If we assume, however, that the butterfly wing is composed of chitin and air, light scattering occurs only at the boundaries of the two substances. Furthermore, according to electromagnetic wave theory, there is a π phase shift when the light is scattered from the chitin-air interface. The first factor means that not the binarized image itself, but its contours has to be Fourier transformed, the second factor means that the chitin-air boundary has to be taken into account with a negative sign. Both factors can be taken into account by taking the derivative of the binarized image in the direction of $\vec{k}$:

TABLE II. Measured and calculated wavelength values corresponding to the maximum reflected intensity for the dorsal and ventral wing surfaces of *Albulina metallica* measured in the backscattered configuration. Peak values calculated from the model are only given for angles where the model is valid.

	0°	15°	30°	45°	60°	75°
Dorsal measured	440	407	397	428	468	
Ventral measured	577	577	534	525	553	604
Ventral Fourier	592	560	539	492	555	607
Ventral model	577			445	545	608

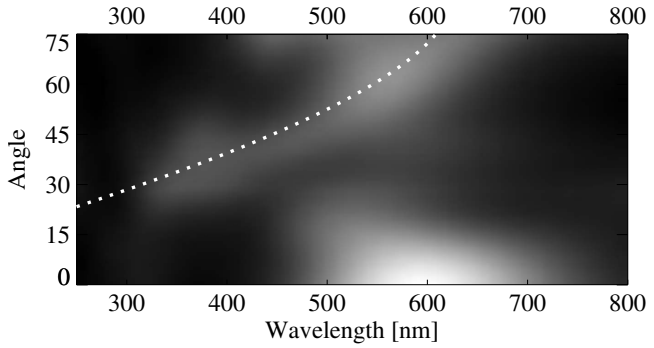

FIG. 12. Theoretical backscattered reflectance spectra calculated from the Fourier power spectrum shown on Fig. 9. The dotted line shows the spectrum calculated for the model in Fig. 8(c).

$$\rho^{high\ \ scattering\ \ centers} = |\nabla_{\vec{k}}\, \mathrm{bin}(\rho^{TEM})|. \tag{7}$$

According to Fourier theory this only means, however, a multiplication with $-\vec{k}$ in Fourier space, i.e., the $I(\lambda)$ spectrum calculated from Eq. (1) has to be replaced with $I(\lambda)/\lambda$, which increases the weight of the shorter wavelength peaks and also slightly shifts the peak positions toward the shorter wavelength.

Butterfly wing scales are often curved. Figure 11 shows a large scale TEM cross section through the wing of the *Albulina metallica* butterfly, several dorsal and ventral side scales are imaged on the "upper" and "lower" side of the wing membrane (denoted by "M" on the image). The largest angles of the scales measured on this image (defined as the angle of the line section connecting two neighboring ridges measured relative to the horizontal side of the image) are −27° for scale "d" and +25° for scale "e" and the standard deviation of the angle distribution is 8°. Hence not only a line cut, but a conical section of width +−8° of the Fourier power spectrum has to be taken into account when calculating the backscattered spectra. This conical section, denoted by α is shown by the two black dashed lines in Fig. 9(b). Figure 12 shows backscattered reflectance spectra calculated using Eq. (7) from the Fourier power spectrum (cf. Figure 9) of the TEM cross section of a ventral scale of the *Albulina metallica* butterfly. The structure of this calculated $I_{calc}(\lambda,\varphi)$ function is indeed similar to the measured one $I_{meas}(\lambda,\varphi)$ shown in Fig. 10: there is a large intensity peak at the normal direction (φ=0), corresponding to the effect of the layer structure and there is a branch with increasing $\lambda_{max}(\varphi)$ for increasing angles. This branch is caused by the presence of the small holes, as explained below. The small holes form layers [cf. Figure 9(a)] and the holes are not completely randomly arranged inside the layers but their RDF has a distinct peak (cf. Figure 5), corresponding to a lateral order of the holes. This peak, in turn, causes the two bars B^- and B^+ to appear in the Fourier image Fig. 9(b). As it is shown in Table II, peak positions thus calculated from the Fourier image match well the measured peak positions. Without the division by λ, (cf. 7), however, the peak positions are at 30–50 nm higher wavelength.

The inset of Fig. 9(b) shows the Fourier image of an idealized structure, where the lateral order is perfect in the layers, but the layers are randomly displaced in the lateral direction. This corresponds to the model shown in Fig. 8(c). The spectrum of this ideal structure can be calculated easily and it is shown by the dotted line in Fig. 12. The point at A^+ corresponds to the layer structure and it causes a peak to appear at $\lambda_{layers}=2n_{eff}d_{layer}$ in the φ=0 (normal) backscattered direction. The lines B^- and B^+ cause a peak to appear in the backscattered direction φ when the vector $\vec{q}$ crosses this line, i.e., $q(\varphi)=q_0/\sin\varphi$, where $q_0=2\pi/d_{lateral}$. Hence the backscattered peak position for φ angle is

$$\lambda(\varphi) = 2n_{eff}d_{lateral}\sin\varphi. \tag{8}$$

This theoretical curve, shown as a dotted line in Fig. 12 matches the trend of the peak positions calculated from the Fourier transform of the TEM section, Fig. 9(b), of the ventral scale, see Table II. (Calculated values for 15° and 30° are not given, the model being unrealistic for these angles. As we can see on Fig. 9(a), the structures $B^{\pm}$ does not extend until such small angles and also for 15° the integrating angle already "samples" structure $A^{\pm}$.) $d_{lateral}$=278 nm was assumed in this calculation, which, taking into account the 62 nm standard deviation (cf. Table I) is a realistic assumption.

VI. CONCLUSIONS

We studied how order-disorder effects present in the chitin-air micro and nanostructure of butterfly wing scales influence their optical properties. As was shown by Prum *et al.* [29], anatomically diverse butterfly scales all produce structural colors by coherent scattering. bidirectional reflectance distribution function of the scales depends on the range of the order present in the structure. Though a short range order is enough [30] to cause a peak in the reflectance spectrum (a color), but long-range order is necessary [18] in order to have a shiny, metallic-like appearance. Fourier analysis is an excellent tool to detect the long-range order, but it is less useful for structures lacking long-range order. The real space averaging method, presented in this paper, can be used for every structure composed of repetitive units. The method is based on the averaging of the local environments of each of the units. We demonstrated this algorithm for three characteristic examples, having long-range order (dorsal scales of the *Cynophrys remus* butterfly), medium-range order (ventral scales of the *Cynophrys remus* butterfly), and short-range order (*Albulina metallica* butterfly).

A structure can deviate from a perfect long-range order in many different ways, i.e., there can be several kinds of randomnesses present in the structure. When the units composing the structure are displaced randomly from their position defined by a perfect ordered lattice, i.e., there is a long-range order "in the background" of the structure, Fourier methods still remain useful, because reciprocal space peaks are only broadened in this case. We have analyzed in detail, how the different kinds of real space disorder influence the shape and width of the reciprocal space peaks. The real space averaging method is particularly useful in case of structures possessing no background lattice, where Fourier analysis is less useful. Optical spectrum of a butterfly scale is closely related to its reciprocal space structure. Indeed, butterfly scales are thin

structures with moderate refractive index contrast, hence, the first Born approximation is applicable. Based on electromagnetic wave theory, we showed that how the results of [29] have to be applied for structures composed of two materials, chitin and air. A detailed analysis of the TEM and SEM images of dorsal and ventral wing scales of the butterfly *Albulina metallica* showed that the scales are composed of spherical air bubbles arranged in layers. The interlayer distance was found to match the intralayer distance of the air holes. These predictions were verified by calculating the theoretical spectra from the Fourier power spectrum utilizing the first Born approximation and a spectrum for an idealized model.

The methods presented in this paper can be successfully utilized in studying the relation of micro-nanostructure and optical properties of not only butterfly wing scales, but also other biological systems possessing structural colors, e.g. avian feather barbs and mammalian skin. But the significance of the methods developed here may be even more far reaching, since these can be well utilized in designing structures with a desired optical effect. Computational electrodynamics [32] can predict the optical properties of a material of known three-dimensional structure with high accuracy, but the simple real and reciprocal space approximation methods exposed in this paper remain useful because of their tractable analytical properties.

ACKNOWLEDGMENTS

This work was supported by EU6 NEST/PATHFINDER/BioPhot-12915. The work in Hungary was partially supported by OTKA under Grants No. 042972 and No. 067793. L.P.B., G.I.M., and Z.V. wish to thank the Hungarian Academy of Sciences and the Belgian FNRS for financial support.

[1] F. E. Nicodemus, J. C. Richmond, J. J. Hsia, I. W. Ginsberg, and T. Limperis, National Bureau of Standards Technical Report, 1977 (unpublished).
[2] J. H. Lambert, *Photometria Sive de Mensure de Gratibus Luminis, Colorum Umbrae* (Eberhard Klett, Augsberg, Germany, 1760).
[3] S. Berthier, *Iridescences: The Physical Colors of Insects* (Springer-Verlag, New York, 2007).
[4] D. G. Stavenga, S. Stowe, K. Siebke, J. Zeil, and K. Arikawa, Proc. R. Soc. London, Ser. B **271**, 1577 (2004).
[5] P. Vukusic, B. Hallam, and J. Noyes, Science **315**, 348 (2007).
[6] P. Vukusic, R. J. Wootton, and J. R. Sambles, Proc. R. Soc. London, Ser. B **271**, 595 (2004).
[7] A. Sweeney, C. Jiggins, and S. Johnsen, Nature (London) **423**, 31 (2003).
[8] R. I. Vane-Wright, Nature (London) **239**, 338 (1972).
[9] J. W. Hall and D. J. Harvey, Zool. J. Linn. Soc. **136**, 171 (2002).
[10] W. Roush, Science **269**, 1816 (1995).
[11] P. Vukusic, J. R. Sambles, and H. Ghiradella, Photonics Sci. News **6**, 61 (2000).
[12] H. Ghiradella, in *Microscopic Anatomy of Invertebrates*, edited by M. Locke (Wiley-Liss, New York, 1998), Vol. 11A, pp. 257–287.
[13] L. P. Biró *et al.*, Phys. Rev. E **67**, 021907 (2003).
[14] E. Yablonovitch, J. Opt. Soc. Am. B **10**, 283 (1993).
[15] R. B. Morris, J. Entomol. Ser. A **49**, 149 (2008).
[16] H. Ghiradella and W. Radigan, J. Morphol. **150**, 279 (1976).
[17] P. Vukusic and J. R. Sambles, Nature (London) **424**, 852 (2003).
[18] K. Kertész, Z. Bálint, Z. Vértesy, G. I. Márk, V. Lousse, J.-P. Vigneron, M. Rassart, and L. P. Biró, Phys. Rev. E **74**, 021922 (2006).
[19] K. Kertész *et al.*, Mater. Sci. Eng., B **149**, 259 (2008).
[20] R. J. D. Tilley and J. N. Eliot, Trans. Lepid. Soc. Japan **53**, 153 (2002).
[21] A. Argyros, S. Manos, M. C. J. Large, D. McKenzie, G. C. Cox, and D. M. Dwarte, Micron **33**, 483 (2002).
[22] M. D. Shawkey, V. Saranathan, H. Pálsdóttir, J. Crum, M. H. Ellisman, M. Auer, and R. O. Prum, J. R. Soc., Interface **6**, S213 (2009).
[23] J.-H. Chen, Y.-C. Lee, M.-T. Tang, and Y.-F. Song, in *Synchrotron Radiation Instrumentation*, American Institute of Physics Conference Series Vol. 879 (AIP, Melville, NY, 2007), pp. 1940–1943.
[24] K. Michielsen and D. G. Stavenga, J. R. Soc. Interface **5**, 85 (2008).
[25] E. Yablonovitch, Phys. Rev. Lett. **58**, 2059 (1987).
[26] C. Jin, X. Meng, B. Cheng, Z. Li, and D. Zhang, Phys. Rev. B **63**, 195107 (2001).
[27] Z. Bálint, A. Kertész, A. Moser, K. Kertész, L. P. Biró, and A. R. Parker, Ann. Hist.-Natur. Mus. Nat. Hung. **101**, 1 (2008).
[28] L. P. Biró, K. Kertész, Z. Vértesy, G. I. Márk, Z. Bálint, V. Lousse, and J. P. Vigneron, Mater. Sci. Eng., C **27**, 941 (2007).
[29] R. O. Prum, T. Quinn, and R. H. Torres, J. Exp. Biol. **209**, 748 (2006).
[30] G. B. Benedek, Appl. Opt. **10**, 459 (1971).
[31] S. Berthier, J. Boulenguez, and Z. Bálint, Appl. Phys. A: Mater. Sci. Process. **86**, 123 (2006).
[32] A. Taflove and S. Hagness, *Computational Electrodynamics: The Finite-Difference Time-Domain Method* (Artech House Publishers, Norwood, MA, 2005).